High thermoelectric power factor in two-dimensional crystals of MoS₂

Kedar Hippalgaonkar,[1,2,3] Ying Wang,[1] Yu Ye,[1] Diana Y. Qiu,[2,4] Hanyu Zhu,[1] Yuan Wang,[1,2] Joel Moore,[2,4]
Steven G. Louie,[2,4] and Xiang Zhang[1,2,*]

[1]*NSF Nano-scale Science and Engineering Center (NSEC), 3112 Etcheverry Hall, University of California, Berkeley, California 94720, USA*
[2]*Material Sciences Division, Lawrence Berkeley National Laboratory (LBNL), 1 Cyclotron Road, Berkeley, California 94720, USA*
[3]*Institute of Materials Research and Engineering, Agency for Science Technology and Research, Singapore, Singapore*
[4]*Department of Physics, University of California, Berkeley, California 94720, USA*

The quest for high-efficiency heat-to-electricity conversion has been one of the major driving forces toward renewable energy production for the future. Efficient thermoelectric devices require high voltage generation from a temperature gradient and a large electrical conductivity while maintaining a low thermal conductivity. For a given thermal conductivity and temperature, the thermoelectric power factor is determined by the electronic structure of the material. Low dimensionality (1D and 2D) opens new routes to a high power factor due to the unique density of states (DOS) of confined electrons and holes. The 2D transition metal dichalcogenide (TMDC) semiconductors represent a new class of thermoelectric materials not only due to such confinement effects but especially due to their large effective masses and valley degeneracies. Here, we report a power factor of MoS₂ as large as 8.5 mW m⁻¹ K⁻² at room temperature, which is among the highest measured in traditional, gapped thermoelectric materials. To obtain these high power factors, we perform thermoelectric measurements on few-layer MoS₂ in the metallic regime, which allows us to access the 2D DOS near the conduction band edge and exploit the effect of 2D confinement on electron scattering rates, resulting in a large Seebeck coefficient. The demonstrated high, electronically modulated power factor in 2D TMDCs holds promise for efficient thermoelectric energy conversion.

I. INTRODUCTION

An ideal thermoelectric material behaves like an electron crystal and phonon glass, allowing a large temperature gradient across it while conducting electricity efficiently to generate a thermoelectric voltage [1]. Significant progress in the thermoelectric performance of materials has been made by exploring ultralow thermal conductivity at high temperature [2] and reducing thermal conductivity by nanostructuring [3], as well as by resonant doping [4] and energy-dependent scattering [5] of electrons. Recently, two-dimensional (2D) transition metal dichalcogenides (TMDCs) have shown unique valley-dependent electronic and optical properties [6–10] and have been theoretically predicted to be superior thermoelectric materials [11–13]. Most theoretical analyses are centered on low lattice thermal conductivity, but the latest calculations suggest that favorable electronic properties of TMDCs also result in an enhanced Seebeck effect [6,14–17], different from gapless, massless carriers in semimetallic graphene [18–22]. Recent experiments have studied the photothermoelectric effect and Seebeck coefficient of monolayer MoS₂ at low carrier densities in the insulating regime, but low electrical conductivity limits the power factor for thermoelectric applications [23,24]. Here, we examine thermoelectric transport in 2D crystals of few-layer MoS₂ at high carrier concentrations in the metallic regime and observe power factors, $S^2\sigma$, as large as 8.5 mW m⁻¹ K⁻² in bilayer MoS₂, where S is the Seebeck coefficient and σ is the electrical conductivity. We use the Seebeck coefficient to probe the 2D density of states (DOS)

in both monolayer and bilayer MoS₂ and show that it agrees well with first principles calculations. Moreover, we show that confinement effects on the electronic DOS and scattering rate enhance the Seebeck coefficient in 2D and that the bilayer in particular has a larger value as a consequence of the higher effective mass and larger valley degeneracy. The 2D TMDCs with high power factors are promising thermoelectric materials for planar applications such as Peltier cooling devices.

II. RESULTS

A. Gate-dependent power factor at room temperature

The Seebeck coefficient and electrical conductivity of 2D MoS₂ are measured as a function of carrier concentration tuned by a back gate (Fig. 1; see also Appendix). The electron concentration is given by $n = C_{ox}/e \cdot (V_g - V_t)$, where C_{ox} is the capacitance between the channel and the back gate, e is the electron charge, and V_g and V_t are the gate and threshold voltage, respectively. The measured electrical conductivities and Seebeck coefficients of monolayer, bilayer, and trilayer MoS₂ follow behavior akin to an extrinsically doped semiconductor, as shown in Fig. 2. The Seebeck voltage is proportional to the asymmetry of occupied DOS around the Fermi level [5,25]. Hence, with increasing electron concentration, the magnitude of the Seebeck coefficient drops as the Fermi level is pushed closer to the conduction band minimum (CBM). However, the measured power factor $S^2\sigma$ increases correspondingly with applied gate voltage V_g due to increasing electrical conductivity, as illustrated in Fig. 3. The bilayer device exhibits the largest power factor $S^2\sigma = 8.5$ mW m⁻¹ K⁻² at $V_g = 104$ V, equivalent to a high electron concentration of $n_{2D} \sim 1.06 \times 10^{13}$ cm⁻².

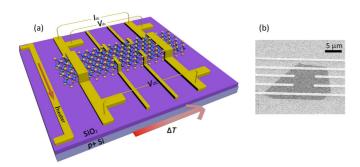*Corresponding author: xiang@berkeley.edu

FIG. 1. (a) Schematic of the simultaneous measurement of the Seebeck coefficient and the electrical conductivity. The illustration shows a monolayer MoS_2, placed on thermally grown SiO_2 on a $p+$ silicon substrate. Two-probe electrical conductivity was measured by passing a current through the device I_{ds} and measuring the drain-source voltage V_{ds} at each temperature. In order to measure the Seebeck coefficient $S = -V_{oc}/\Delta T$, current was passed through the heater to generate a temperature gradient ΔT while the open-circuit voltage V_{oc} was measured. (b) Scanning electron micrograph of an actual device as described in (a). The hall-bar electrodes were used to obtain the ratio of the two-probe to the four-probe electrical conductivities $\gamma_c = \sigma_{4p}/\sigma_{2p}$ to estimate the contribution due to contact resistance at each temperature. For the monolayer sample, $\gamma_c = 1.98$ at 300 K.

The magnitude of the power factor is expected to reach a peak and then drop for even higher carrier concentrations as the increasing electrical conductivity is offset by the decreasing Seebeck coefficient [5]. However, for our MoS_2 samples, the power factor does not peak, as this optimum carrier concentration is expected to occur at an even higher gate voltage ($n_{2D} \sim 1.31 \times 10^{13}$ cm^{-2}, equivalent to a bulk concentration of $n_{3D} \sim 1 \times 10^{20}$ cm^{-3}, obtained by considering a bilayer thickness of 1.3 nm), which is limited by the electrical breakdown of the gate oxide in our experiment, as shown for a couple of devices in the Supplemental Material [26] and discussed in Ref. [27].
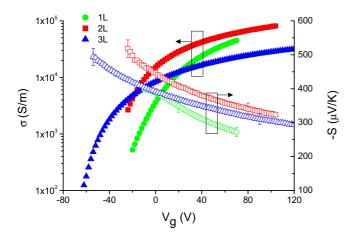

FIG. 2. Electrical conductivities σ (closed markers, error bars inclusive) and Seebeck coefficients S (open markers, error bars as indicated) as a function of gate voltage at 300 K for monolayer MoS_2 (green circles), bilayer MoS_2 (red squares), and trilayer MoS_2 (blue triangles). As the carrier concentration $n \propto (V_g - V_t)$ increases, σ increases and the magnitude of S decreases. S is negative, which confirms that the sample is n-type.
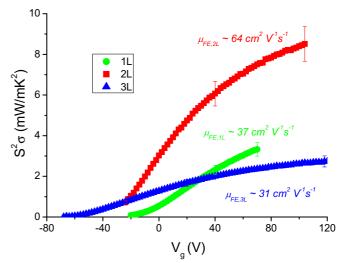

FIG. 3. Power factor $S^2\sigma$ (representative error bars illustrated) as a function of V_g. The bilayer device with a larger effective mobility of 64 cm^2 V^{-1} s^{-1} exhibits a maximum power factor of 8.5 mW m^{-1} K^{-2} at $n = 1.06 \times 10^{13}$ cm^{-2} at room temperature, twice that of commercially used bulk Bi_2Te_3.

The effective mobilities are determined by a standard transistor measurement, as shown in Fig. 4. The measured effective mobilities at room temperature are 37 cm^2 V^{-1} s^{-1} for the monolayer and 64 cm^2 V^{-1} s^{-1} for the bilayer. The bilayer sample shows the largest electrical conductivity, as well as the highest Seebeck coefficient. Our samples are exfoliated from natural molybdenite crystals, so their initial dopant and impurity levels vary. Hence, the device mobilities differ from sample to sample and are lower than the theoretical estimate ($\sim$410 cm^2 V^{-1} s^{-1}) [28], which could be due to extrinsic effects such as screening and scattering from the underlying dielectric substrate [16] and impurity levels in individual samples [29]. For phonon-limited theoretical mobility in
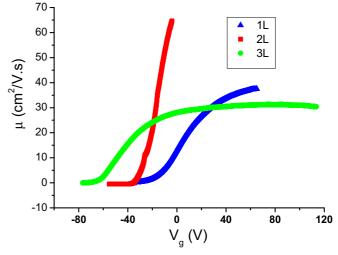

FIG. 4. The measured field-effect mobilities of monolayer, bilayer, and trilayer samples as a function of back gate voltage V_g. The measured mobility is 37 cm^2 V^{-1} s^{-1} for the monolayer, 64 cm^2 V^{-1} s^{-1} for the bilayer, and 31 cm^2 V^{-1} s^{-1} for the trilayer.
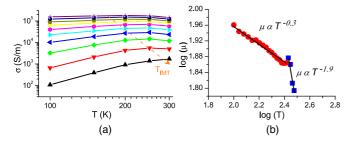
FIG. 5. (a) Conductivity as a function of temperature: high ($n = 5 \times 10^{12}$ cm^{-2} at the top) to low ($n = 4 \times 10^{11}$ cm^{-2} at the bottom) carrier concentration. As the gate voltage (carrier concentration) decreases, the insulator-to-metal transition temperature T_{IMT} shifts to higher temperatures (indicated by the dotted arrow). (b) Temperature-dependent mobility of monolayer MoS$_2$. The mobility undergoes a rapid decrease with an exponent $\sim$0.3 to $\sim$1.9 crossing T_{IMT}.

suspended monolayer MoS$_2$, a power factor as large as 28 mW m^{-1} K^{-2} is predicted at $n_{2D} = 1 \times 10^{12}$ cm^{-2} [13]; therefore, in principle, the power factor of 2D MoS$_2$ can be improved further by making cleaner samples to obtain higher mobility closer to the theoretical limit.

B. Temperature-dependent transport in monolayer MoS$_2$

At high temperatures and high electron concentrations, when the Fermi level is pushed close to the conduction band edge, monolayer MoS$_2$ undergoes an insulator-to-metal transition [14–16]. This metallike regime for conducting MoS$_2$ is determined by analyzing the conductivity as a

function of temperature for different electron concentrations (gate voltages): we study the temperature-dependent electrical conductivity from 1.0×10^{11} to 5.1×10^{12} cm^{-2} for a monolayer MoS$_2$ sample, as plotted in Fig. 5(a). The insulator-to-metal transition temperature T_{IMT} is defined as the temperature at which the measured conductivity changes from increasing with temperature to a metallike decrease with temperature. This is corroborated from the mobility as a function of temperature, which changes its slope from 0.3 to $\sim$1.9 at the insulator-to-metal transition temperature shown in Fig. 5(b). We thus illustrate the electronic phase diagram of transport in MoS$_2$ in Fig. 6(a), where T_{IMT} is plotted as a function of the carrier concentration. Since this phase diagram is linked to percolation, in the insulating phase, the conductivity follows a relation in temperature given by $\sigma \propto \exp(-(T_0/T)^{1/3})$ in a 2D system, which fits a Mott variable range hopping (m-VRH) model [16,29,30], separate from the first-order transition described elsewhere [14,31]. Figure 6(b) shows the measured Seebeck coefficient, which follows a monotonic increase with temperature as $S \propto T^{1/3}$, using Zyvagin's formula for the m-VRH model [32–34], with $S \to 0$ as $T \to 0$ (inset). A similar m-VRH transport phenomenon has been observed in chemical vapor deposition (CVD)-grown MoS$_2$ for the insulating phase [23], in stark contrast with the thermally activated transport mechanism in semiconductors [35,36]. Therefore, from the electronic phase diagram in Fig. 6(a) for high temperatures ($T > 250$ K) and large electron concentrations ($n > 2 \times 10^{12}$ cm^{-2} at 300 K), electrical transport in MoS$_2$ is metallike and the Mott relation for calculation of the Seebeck coefficient holds. The doping level is not high enough to observe metallic transport behavior at lower temperatures.
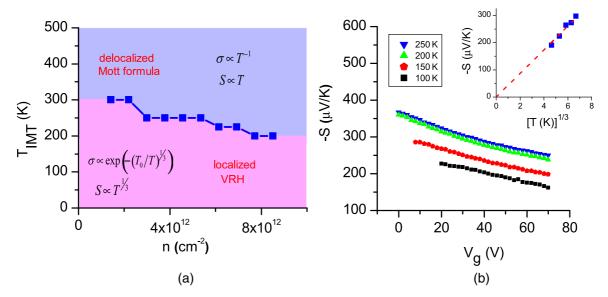

FIG. 6. (a) Phase diagram for thermoelectric transport as a function of temperature and electron concentration. For the metallic phase $T > T_{IMT}$, electrical conductivity decreases with temperature $\sigma \propto T^{-1}$ and the Seebeck coefficient increases slowly $S \propto T$ (Mott formula for extended states). In the insulating phase $T < T_{IMT}$, m-VRH for localized states dictates transport, resulting in $\sigma \propto \exp(-(T_0/T)^{1/3})$ (see Supplemental Material [26]) and $S \propto T^{1/3}$. (b) Experimental Seebeck coefficient for monolayer MoS$_2$ as a function of temperature and applied back gate voltage. The magnitude of Seebeck coefficient decreases with V_g and increases with temperature. In the inset, we show measured Seebeck coefficient at a fixed carrier concentration $n = C_{ox}/e \cdot (V_g - V_t)$, which follows a function of $T^{1/3}$, indicating a m-VRH (localized) regime in the temperature range 100–250 K (further details in Supplemental Material [26]). At all temperatures, the experimental Seebeck coefficient at a fixed carrier concentration $V_g - V_t$ is considered.
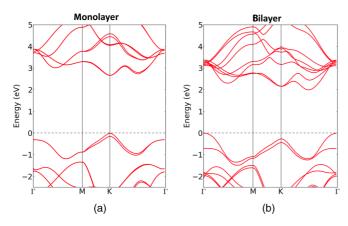
FIG. 7. QP band structure of pristine (a) monolayer and (b) bilayer MoS$_2$ calculated at the GW level.

C. Nature of scattering in monolayer and bilayer MoS$_2$

High power factors in 2D MoS$_2$ have been predicted to stem from large conduction band effective masses, leading to a large Seebeck coefficient [13]. In order to better understand the origin of the large magnitude for monolayer and bilayer MoS$_2$, we calculate the Seebeck coefficient from the linearized Boltzmann transport equation (BTE) under the relaxation time approximation, given by the following:

$$S = \frac{1}{qT} \frac{\int_{E_c}^{\infty} \frac{df_{FD}}{dE} D_{2D}(E).(E - E_F).\tau(E)dE}{\int_{E_c}^{\infty} \frac{df_{FD}}{dE} D_{2D}(E).\tau(E)dE} \tag{1}$$

Here, f_{FD} is the Fermi Dirac distribution, $D_{2D}(E)$ is the 2D DOS, E_F is the Fermi level with respect to the CBM at E_c, q is the electron charge, and $\tau(E) = \tau_0 E^r$ is the energy-dependent relaxation time, where r is the scattering exponent and depends on the dominant scattering mechanism [37].

1. Calculating effective mass and DOS in monolayer and bilayer MoS$_2$

In order to obtain the DOS used earlier in Eq. (1), we performed first principles calculations of the quasiparticle (QP) band structure of suspended monolayer and bilayer MoS$_2$ within the GW approximation [38]. The CBM was found to be at the K and K' points in the Brillouin zone for monolayer MoS$_2$ and along the sixfold degenerate Λ high-symmetry line (Λ valley) for bilayer MoS$_2$, in good agreement with previous calculations [39–41]. The computed DOS of pristine monolayer and bilayer MoS$_2$ at the GW level shows that due to the larger band effective mass and higher degeneracy in

the Λ valley, the DOS of bilayer MoS$_2$ at the CBM is ~4 times larger than the DOS of monolayer MoS$_2$. We included the Mo semicore $4d, 4p$, and $4s$ states as valence states for our density functional theory (DFT) and GW calculations. The theoretical band structure and DOS calculations were done in a supercell arrangement with a plane-wave basis using norm-conserving pseudopotentials with a 125-Ry wave function cutoff. The distance between repeated supercells in the out-of-plane direction was 25 Å. We fully relaxed the monolayer and bilayer MoS$_2$ structures and included spin-orbit (SO) interactions as a perturbation [42,43]. The dielectric matrix was calculated on a $60 \times 60 \times 1$ q-point grid with a 25-Ry energy cutoff. The 2500 bands were included in the summation over empty states. Dynamical effects in the screening were included with the Hybertsen-Louie generalized plasmon pole (HL-GPP) model [38].

The calculated QP band structures of monolayer and bilayer MoS$_2$ are shown in Fig. 7. We find that monolayer MoS$_2$ has a direct band gap at the K point. In addition to the CBM at K, there is another valley in the conduction band along the Λ high-symmetry line from Γ to K. We find that the bottom of this Λ valley is 67 meV higher in energy than the K point and thus unlikely to contribute to the Seebeck coefficient at room temperature. We also find that SO coupling splits the conduction band at K by 2 meV, so we expect both spin bands to contribute to the transport. We further determine that the effective mass of the lower band (which we refer to as spin up) is 0.45 m_0 and the effective mass of the upper band (which we refer to as spin down) is 0.59 m_0, where m_0 is the free electron mass. For bilayer MoS$_2$, we ascertain that the CBM occurs along the Λ high-symmetry line. This Λ valley is anisotropic, and its average effective mass is 0.68 m_0. Calculated effective masses, SO splitting of the conduction band, and ordering of the conduction band valleys are summarized in Table I. As expected for parabolic bands in 2D, we observe that the DOS is a step function at the conduction band edge in both cases [Fig. 8(a) and 8(b); the broadening seen in the figures results from a numerical 20-meV broadening in the calculation]. Thus, in estimating the Seebeck coefficient from Eq. (1), we assume that the DOS is constant, given by the value of the DOS at the step edge [dotted vertical lines in Fig. 8(a) and 8(b)] and hence energy independent.

Finally, we explore the possibility that carrier doping, which is known to renormalize the QP band gap, might also change the QP effective masses. We performed an additional GW calculation on doped monolayer MoS$_2$, with a carrier concentration of $n = 1 \times 10^{13}$ cm^{-2}. We found that the QP effective mass of the spin-up band in the K valley is unchanged for the spin-up band, while the effective mass of the spin-down band decreases by 10%. Thus, the average carrier effective

TABLE I. Comparison of (1) the difference between the CBM at K and that along the Λ high-symmetry line ($E_K - E_\Lambda$), (2) SO splitting of the conduction band at K, and (3) effective masses for spin-up ($\uparrow$) and spin-down ($\downarrow$) states in the K and Λ valleys in units of the free electron mass (m_0) for monolayer and bilayer MoS$_2$ with different doping levels (n).

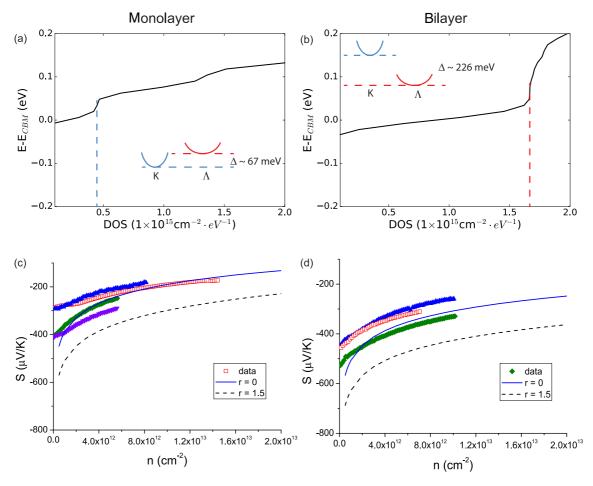|	n (cm^{-2})	$E_K - E_\Lambda$(eV)	$E_{K,c\downarrow} - E_{K,c\uparrow}$(eV)	$m_{K\uparrow}(m_0)$	$m_{K\downarrow}(m_0)$	$m_{\Lambda\uparrow}(m_0)$	$m_{\Lambda\downarrow}(m_0)$
Monolayer	0	−0.067	0.003	0.45	0.59	0.87	0.73
Monolayer	1×10^{13}	−0.668	0.003	0.45	0.53	1.18	1.02
Bilayer	0	−0.226	0.000	0.67	0.67	0.68	0.68

FIG. 8. Calculated DOS of pristine (a) monolayer MoS$_2$ plotted as a function of the energy difference from the CBM in the K valley and (b) bilayer MoS$_2$ plotted as a function of the energy difference from the CBM in the Λ valley. The step function feature expected from 2D confinement can be seen clearly and is used to estimate the constant DOS (dotted vertical lines) used in Eq. (1). In the inset, the relative positions of the K and Λ valleys in monolayer and bilayer MoS$_2$ show that thermoelectric transport only occurs through the K point in the monolayer and only occurs through the Λ high-symmetry direction in the bilayer, since the energy difference is $> \sim 2k_B T$ in both cases. (c) Monolayer and (d) bilayer experimental data (open symbols) compared with the estimated Seebeck coefficient from Eq. (1) for $r = 0$, consistent with phonon-limited scattering in 2D (solid lines) and $r = 1.5$ for reference (dashed lines). The data fit the $r = 0$ phonon-limited scattering case well.

mass decreases by $\sim 0.08\, m_0$ as the doping is increased from 0 to $n = 1 \times 10^{13}$ cm^{-2}.

2. Calculation of Seebeck coefficient and Fermi level with respect to the CBM

In order to calculate the Seebeck coefficient for the monolayer and bilayer samples, the position of the Fermi level E_f with respect to the CBM E_c, given by $E_f - E_c$, must be known. Given that doping due to the back gate pushes the 2D MoS$_2$ channels into the degenerate limit (evidenced by the decreasing conductivity with temperature and the linearity of the measured Seebeck coefficient as a function of temperature), Fermi-Dirac statistics need to be used. Boltzmann statistics are only valid in the limit that $|E_c - E_f| \gg k_B T$, which is not the case in our experiments at high carrier concentrations.

Therefore, in the degenerate limit,

$$n = \int_{E_c}^{\infty} D_{2D}(E) f_{FD}(E) \, dE \tag{2}$$

where $D_{2D}(E) = \frac{g_v g_s m^*}{2\pi \hbar^2}$ are the 2D DOSs ascertained earlier. Here, g_v and g_s are the valley and spin degeneracies, respectively, and m^* is the band effective mass obtained from the band structure. A summary of the values for monolayer and bilayer MoS$_2$ is given in Table II. $f_{FD}(E) = \frac{1}{e^{(E-E_f)/k_B T}+1}$ is the Fermi-Dirac distribution. Let $\varepsilon = (E - E_c)/k_B T$ and $\eta = (E_F - E_c)/k_B T$. Then, Eq. (2) gives $n_{2D} = N_{c,2D} \int_0^\infty f_{FD}(\varepsilon) d\varepsilon$, where $N_{c,2D} = D_{2D} . k_B T$ is the effective DOS in two dimensions. Here, $\int_0^\infty f_{FD}(\varepsilon) d\varepsilon = F_0(\eta)$ is the zeroth-order Fermi integral, which can be evaluated analytically as $F_0(\eta) = \ln(1 + e^\eta)$.

Therefore, in order to relate the Fermi energy to the carrier density, we use the expression $(E_F - E_c) = k_B T (e^{n/N_c} - 1)$, where n is determined experimentally in the 2D MoS$_2$ channel.

Calculating the Seebeck coefficient as a function of the carrier concentration, n, elucidates the dominant scattering mechanism of electrons in the 2D MoS$_2$ channels given by Eq. (1). Using the energy-independent DOS D_{2D} and accounting for the energy-dependent scattering rate, Eq. (1)

TABLE II. Summary of band structure calculations obtained from pristine monolayer and bilayer MoS_2 used for the estimation of the Seebeck coefficient using Eq. (1).

	Monolayer	Bilayer
Valley degeneracy, g_v	2	6
Spin degeneracy, g_s	2	2
Effective mass, m^*	$(0.45 + 0.59)/2m_0 \sim 0.52 m_0$	$0.68\,m_0$
	at the K point CBM	at the Λ point CBM
DOS, D_{2D}	$4.33 \times 10^{14} cm^{-2} eV^{-1}$	$17.0 \times 10^{14} cm^{-2} eV^{-1}$

can be written as follows:

$$S = -\frac{k_B}{q}\left[\eta - \frac{(r+2)\int_0^\infty f_{FD}\varepsilon^{r+1}d\varepsilon}{(r+1)\int_0^\infty f_{FD}\varepsilon^r d\varepsilon}\right] \qquad (3)$$

For scattering of acoustic phonons, it has been shown that $\tau(E)$ scales with the DOS [44]; thus, $r = 0$ for acoustic phonon-limited scattering in 2D in the single parabolic band model. For charged impurity scattering, the scattering roughly has the energy dependence $r = 3/2$ for a simple model for elastic scattering in which the bands are assumed to be parabolic and the impurity is screened with a Thomas-Fermi type screening in 2D [44]. Typically, $r = 3/2$ is the exponent for electrons scattered by charged impurities in three dimensions, but it can be different for two dimensions depending on the approximations used [37,44,45]. We calculate the Seebeck coefficient for both monolayer and bilayer MoS_2 as a function of the carrier concentration and compare the calculated Seebeck coefficient to experimental values for four devices [Fig. 8(c) and 8(d), respectively]. Numerical integration was performed using the function fermi.m in Matlab [46]. Here, we see that the Seebeck coefficient, as calculated from Eq. (3), fits the experimental data quite well when $r = 0$, which is consistent with phonon-limited scattering in 2D and captures the relative change in the Seebeck coefficient as a function of the carrier concentration induced by the back gate voltage. Finally, our calculations show that given identical carrier concentrations, the magnitude of the Seebeck coefficient for the bilayer is larger than that for the monolayer as a consequence of the larger DOS at the conduction band edge, which stems from both a heavier effective mass and a higher valley degeneracy of the CBM at the high-symmetry Λ valley.

Here, the value of the Seebeck coefficient does not depend on the absolute value of the scattering time τ. Hence, while the mobility of the samples measured is limited directly by the scattering time, given by $\mu = e\tau/m^*$, the Seebeck coefficient is only sensitive to the availability of the DOS near the Fermi energy and the energy dependence of the scattering term.

Comparing the experimentally measured Seebeck coefficient to theory strongly suggests that the scattering is dominated by electron-phonon scattering. The electron-phonon scattering rate in the monolayer has been previously calculated from first principles [27,47]. Over an energy range of 50 meV, the scattering rate in both the K and Λ valleys is constant, with a total scattering rate of roughly 1×10^{13} s^{-1} over all phonon modes. However, the mobilities in our samples are lower than the intrinsic phonon-limited mobility of ~ 410 cm^2 V^{-1} s^{-1} [28]. Our measured mobilities are similar to other measured mobilities for MoS_2 on SiO_2 [14,17], suggesting that substrate-

monolayer coupling may significantly alter the phonon channels available to carriers in MoS_2.

III. DISCUSSION

The Seebeck coefficient is given by integrating the energy-dependent relaxation time modulated by a window function defined by $F_{w1}(E,T) = (E - E_F) \times \{-d f_{FD}(E,T)/dE\}$, where E_F is the Fermi level and $f_{FD}(E,T)$ is the Fermi-Dirac distribution [48]. This function is odd around E_F, with a width of $\sim 2k_B T$ [49]. For doped, metal-like 2D MoS_2, as the Fermi level approaches the bottom of the conduction band within this energy width of the window function, the rapidly changing DOS [Fig. 8(a) and 8(c)] generates a large asymmetry around the Fermi level, which leads to an enhanced value of the Seebeck coefficient [50,51]. This effect is exacerbated by the large transport effective mass (m_d^*), which includes the valley and spin degeneracies. In three dimensions, $m_d^* = (g_v \cdot g_s)^{2/3} \times m^*$ [1,49]. In two dimensions, $m_d^* = (g_v \cdot g_s) \times m^*$. For monolayer MoS_2, $g_v = g_s = 2$; thus, the DOS effective mass contributing to transport is $m_{d,1L}^* \sim 2.1\,m_0$. Bilayer MoS_2 has $g_v = 6$ and $g_s = 2$, giving $m_{d,2L}^* \sim 8.1\,m_0$. These values are significantly larger than conventional thermoelectric materials and are the main reason for our large measured Seebeck coefficients.

The fits to the Seebeck coefficient in Fig. 8(c) and 8(d) using the full Fermi-Dirac distributions are accurate for carrier concentrations higher than $n \sim 2 \times 10^{12}$ to 4×10^{12} cm^{-2}, which is consistent with the phase diagram in Fig. 6(a). At lower temperatures and lower carrier concentrations, m-VRH transport is determined by a localization length up to $n \sim 2 \times 10^{12}$ cm^{-2} (see Supplemental Material [26]). Band gap renormalization in monolayer MoS_2 at high doping levels ($\sim 1 \times 10^{13}$ cm^{-2}) causes the average effective mass to decrease slightly with doping concentration, thus explaining the slight drop in the measured Seebeck coefficient at high carrier concentrations in Fig. 8(c). Notwithstanding these minor effects, the scattering exponent ($r = 0$) determined from fitting the calculated Seebeck coefficients to the experimental data and the exponent of the temperature-dependent mobility at high temperatures prove that transport in supported, doped 2D MoS_2 (and probably more generally in TMDCs) is limited by phonon scattering at high temperatures.

Despite the excellent agreement of the experimental and theoretical Seebeck coefficients, our measured field-effect mobility is still much lower than the calculated, intrinsic value of 410 cm^2 V^{-1} s^{-1} [28], because in the calculation of the intrinsic mobility, the total scattering rate is obtained as a sum over all phonon channels only in pristine monolayer

MoS_2. It's not surprising, in our case, that the substrate would add additional scattering channels, thus reducing the mobility further. Intriguingly, because the Seebeck coefficient depends not on the energy-independent magnitude of the scattering time τ_0 but only on the energy-dependent exponent r, there are many avenues to improve the measured power factor further by judiciously picking substrates with weak phonon coupling, as well as improving the quality of the MoS_2 channel. The magnitude of the Seebeck coefficient is expected to be even larger when the relaxation time has energy dependence with $r > 0$ [$r = 1.5$ is plotted for reference in Fig. 8(c) and 8(d)], so engineering the dielectric environment to change the dominant scattering mechanism is another possible route to enhance the power factor. Like MoS_2, other TMDCs [52] and phosphorene [53,54] are expected to simultaneously have large band effective masses and mobilities, possibly leading to high values of the power factor and thus highlighting 2D semiconductor crystals as potential thermoelectric materials. It remains to be seen whether the thermal conductivity of these materials can be tuned further, making them directly useful for thermoelectric applications by enhancing the thermoelectric figure-of-merit ZT, although a high power factor itself can be utilized for in-plane Peltier cooling [55].

IV. CONCLUSIONS

Our experiments report the thermoelectric properties of exfoliated 2D crystals of MoS_2, and we observe high power factors as large as 8.5 mW m^{-1} K^{-2} at room temperature. This is twice as high as commonly used bulk Bi_2Te_3, making 2D TMDCs promising candidates for planar thermoelectric applications. The enhanced power factor in the metallic regime is attributed to the sizable conductivity in the highly doped crystals and a large Seebeck coefficient stemming from high valley degeneracies and effective masses, especially in the case of the bilayer, where a large effective mass at the CBM in the Λ valley is coupled with a sixfold valley degeneracy. We measure thermoelectric transport in the highly doped regime allowing us to access the 2D DOS in TMDCs. Our device configuration allows us to tune the carrier concentration of 2D MoS_2, which is difficult in bulk materials, hence providing important insights into thermoelectric transport in these layered materials. The high power factor in layered TMDCs provides an exciting avenue to enhance thermoelectric efficiencies and galvanize the growth of thermoelectric devices in the near future.

During the review process, it came to our attention that a similar paper has been published in Ref. [56] with conclusions comparable to what we've obtained, although the effect of increased degeneracy in the bilayer and the origin of the enhanced Seebeck coefficient is not considered in their paper.

ACKNOWLEDGMENTS

APPENDIX: SAMPLE PREPARATION, CHARACTERIZATION, AND MEASUREMENT DETAILS

Exfoliated samples are obtained using the Scotch tape method by cleaving bulk molybdenite. We exfoliate the samples onto 275-nm thermally grown SiO_2 on a highly doped p-Si substrates. MoS_2 flakes are visible on the sample under an optical microscope, and the monolayer, bilayer, or trilayer samples are selected based on characterization using optical contrast, photoluminescence imaging, and Raman spectroscopy (see Supplemental Material [26]). Layer thicknesses for monolayer and bilayer devices are measured with atomic force microscopy (AFM) for fabricated samples. Defective samples with cracks, ripples, and/or folds are identified with high-resolution scanning electron microscopy (HR-SEM) and are not used for measurements (see Supplemental Material [26]).

The heating element is a resistive metal line, through which a direct current (dc) current I_{dc} up to 20 mA is applied. The heat generated from the heater line creates a temperature gradient across the TMDC sample, given by $Q \propto I_{dc}^2 R_{htr} \propto \Delta T$. The electrodes patterned on two sides of the sample function as probes for both electrical measurements and local temperature measurement. For each electrode, the resistance is given by $R_{hot/cold} \propto T_{hot/cold}$. Then, the temperature difference across the device is calibrated as $\Delta T = T_{hot} - T_{cold}$, where $R_{hot/cold} = \alpha_{hot/cold}/T_{hot/cold}$ obtained at every global temperature, with the slope $\alpha_{hot/cold}$ determined experimentally. The open-circuit voltage across the device V_{oc} as a function of heating current is then determined, from which the Seebeck coefficient of the device can be deduced as $S = -V_{oc}/\Delta T$.

In order to minimize the electrical contact resistance, we use Ti/Au films evaporated with electron beam evaporation. Titanium has been known to have good Fermi level alignment with monolayer MoS_2 [31]. In order to improve the contact quality, we annealed the sample *in situ* at 475 K for 1 h in the cryostat prior to performing measurements. After annealing, all of our current-voltage (I-V) curves are linear, indicating ohmic contact; hence, none of the transport characteristics can be ascribed to Schottky behavior. It has been reported that the contact resistance contribution to measured total resistance at room temperature can be as large as 50% at 100 K with Ti/Au contacts [31]. In our case, we define the ratio of the four-probe to two-probe conductivity as the contact ratio γ_c, which is 2 at 300 K and 2.5 at 100 K. Hence, our estimation of the intrinsic electrical conductivity of the layered MoS_2 is underestimated due to included contact resistance. The Seebeck measurements are not affected by the contact quality since they are measured in an open-circuit configuration. However, the measured S is a sum of the sample and the contacts (Ti/Au). Since the metallic Seebeck coefficient is $< 1 \, \mu$VK^{-1} at all temperatures, it does not affect our measurements and we do not consider it in our estimation. The effects of joule heating, current crowding, and thermoelectric potentials due to current flow in the 2D devices [57,58] are negligible, since the current densities used for electrical conductivity measurements are

very small: $I_{ds} < 0.1\,\mu A/\mu m$ (see Supplemental Material [26]). All measurements were performed in vacuum at 2×10^{-6} torr. For lower gate voltages close to the threshold voltage V_t, the channel resistance becomes too high and we are unable to measure the Seebeck coefficient accurately. The maximum gate voltages V_g applied for all devices are limited by the electrical breakdown of the gate oxide. In order to determine identical carrier concentrations n for different devices, we determined the threshold voltage V_t by linear extrapolation of the transfer curve (I_{ds} vs V_g). Since each device has a different V_t, the gate voltage at which the power factor is considered (for same carrier concentration) is also different for each device. The highly doped silicon wafer (the back gate) acts as a heat sink that controls the temperature gradient across the two electrodes, while the low thermal conductivity SiO_2 (gate dielectric) acts as a thermal barrier between the bottom wafer and the metal electrodes, controlling the actual local temperatures. The heat is generated from the center of the patterned heater and decays linearly on the surface of the SiO_2 upon which the MoS_2 lies, while the metal electrodes that function as resistance thermometers measure the local temperature gradient in intimate contact with the MoS_2. The heat flows out from the electron-beam lithography (EBL)-defined heater isotropically in all directions in the SiO_2 substrate. Since the MoS_2 is atomically thin, a very small portion of the heat generated by the heater flows through the MoS_2 cross section. The key to accurate Seebeck measurement of the MoS_2 lies in measuring the local temperature across the MoS_2 at the same locations as the open-circuit voltage, which the design is able to accomplish. The high resistance in the off state of the $MoS_2(V_g \leqslant V_t)$ introduces additional capacitive coupling; hence, the noise levels of the Seebeck coefficient measured are higher. We do not measure the Seebeck coefficient in the off state in this paper.

---

[1] C. Slack, in *CRC Handbook of Thermoelectrics*, edited by D. M. Rowe (CRC Press, Boca Raton, 1995), pp. 407–440.

[2] L.-D. Zhao, S.-H. Lo, Y. Zhang, H. Sun, G. Tan, C. Uher, C. Wolverton, V. P. Dravid, and M. G. Kanatzidis, Nature **508**, 373 (2014).

[3] A. I. Hochbaum, R. Chen, R. D. Delgado, W. Liang, E. C. Garnett, M. Najarian, A. Majumdar, and P. Yang, Nature **451**, 163 (2008).

[4] J. P. Heremans, V. Jovovic, E. S. Toberer, A. Saramat, K. Kurosaki, A. Charoenphakdee, S. Yamanaka, and J. G. Snyder, Science **321**, 554 (2008).

[5] D. M. Rowe, *Thermoelectrics Handbook: Macro to Nano* (Taylor & Francis, CRC Press, Boca Raton, 2005).

[6] B. Radisavljevic, A. Radenovic, J. Brivio, V. Giacometti, and A. Kis, Nat. Nanotechnol. **6**, 147 (2011).

[7] Q. H. Wang, K. Kalantar-Zadeh, A. Kis, J. N. Coleman, and M. S. Strano, Nat. Nanotechnol. **7**, 699 (2012).

[8] T. Cao, G. Wang, W. Han, H. Ye, C. Zhu, J. Shi, Q. Niu, P. Tan, E. Wang, B. Liu, and J. Feng, Nat. Commun. **3**, 887 (2012).

[9] K. F. Mak, K. He, C. Lee, G. H. Lee, J. Hone, T. F. Heinz, and J. Shan, Nat. Mater. **12**, 207 (2013).

[10] D. Y. Qiu, T. Cao, and S. G. Louie, Phys. Rev. Lett. **115**, 176801 (2015).

[11] W. Huang, X. Luo, C. K. Gan, S. Y. Quek, and G. Liang, Phys. Chem. Chem. Phys. **16**, 10866 (2014).

[12] D. Wickramaratne, F. Zahid, and R. K. Lake, J. Chem. Phys. **140**, 124710 (2014).

[13] H. Babaei, J. M. Khodadadi, and S. Sinha, Appl. Phys. Lett. **105**, 193901 (2014).

[14] B. Radisavljevic and A. Kis, Nat. Mater. **12**, 815 (2013).

[15] Z. Yu, Y. Pan, Y. Shen, Z. Wang, Z.-Y. Ong, T. Xu, R. Xin, L. Pan, B. Wang, L. Sun, J. Wang, G. Zhang, Y. W. Zhang, Y. Shi, and X. Wang, Nat. Commun. **5**, 5290 (2014).

[16] W. Zhu, T. Low, Y.-H. Lee, H. Wang, D. B. Farmer, J. Kong, F. Xia, and P. Avouris, Nat. Commun. **5**, 3087 (2014).

[17] S. Kim, A. Konar, W.-S. Hwang, J. H. Lee, J. Lee, J. Yang, C. Jung, H. Kim, J.-B. Yoo, J.-Y. Choi, Y. W. Jin, S. Y. Lee, D. Jena, W. Choi, and K. Kim, Nat. Commun. **3**, 1011 (2012).

[18] K. Novoselov, A. Geim, S. Morozov, D. Jiang, Y. Zhang, S. Dubonos, I. Grigorieva, and A. Firsov, Science **306**, 666 (2004).

[19] A. H. C. Neto, F. Guinea, N. Peres, K. Novoselov, and A. Geim, Rev. Mod. Phys. **81**, 109 (2009).

[20] Y. M. Zuev, W. Chang, and P. Kim, Phys. Rev. Lett. **102**, 096807 (2009).

[21] F. Ghahari, H.-Y. Xie, T. Taniguchi, K. Watanabe, M. S. Foster, and P. Kim, Phys. Rev. Lett. **116**, 136802 (2016).

[22] Graphene, which is a prototypical 2D material, has exhibited larger power factors of $\sim$10 mW m^{-1} K^{-2} due to novel correlated effects, but its thermoelectric applications are limited by an extremely high thermal conductivity.

[23] J. Wu, H. Schmidt, K. K. Amara, X. Xu, G. Eda, and B. Özyilmaz, Nano Lett. **14**, 2730 (2014).

[24] M. Buscema, M. Barkelid, V. Zwiller, H. S. J. Van Der Zant, G. A. Steele, and A. Castellanos-Gomez, Nano Lett. **13**, 358 (2013).

[25] B. Bhushan, *Springer Handbook of Nanotechnology* (Springer-Verlag, Berlin, Heidelberg, 2007).

[26] See Supplemental Material at http://link.aps.org/supplemental/10.1103/PhysRevB.95.115407 for power factor saturation at higher carrier concentrations, details on field-effect mobility measurements, analysis of m-VRH transport in the insulating phase of monolayer MoS_2, layer thickness and quality characterization, effect of contacts and comparison to other thermoelectric materials.

[27] G. J. Snyder and E. S. Toberer, Nat. Mater. **7**, 105 (2008).

[28] K. Kaasbjerg, K. S. Thygesen, and K. W. Jacobsen, Phys. Rev. B **85**, 115317 (2012).

[29] S. Ghatak, A. N. Pal, and A. Ghosh, ACS Nano **5**, 7707 (2011).

[30] S. Lo, O. Klochan, C. Liu, W. Wang, A. R. Hamilton, and C.-T. Liang, Nanotechnology **25**, 375201 (2014).

[31] B. W. H. Baugher, H. O. H. Churchill, Y. Yang, and P. Jarillo-Herrero, Nano Lett. **13**, 4212 (2013).

[32] P. Zvyagin, Phys. Status Solidi **58**, 443 (1973).

[33] S. V. Demishev, M. V. Kondrin, A. A. Pronin, N. E. Sluchanko, N. A. Samarin, A. G. Lyapin, and G. Biscupski, J. Exp. Theor. Phys. Lett. **68**, 842 (1998).

[34] M. J. Burns and P. M. Chaikin, J. Phys. C Solid State Phys. **18**, L743 (1985).

[35] B. Jalan and S. Stemmer, Appl. Phys. Lett. **97**, 42106 (2010).

[36] K. P. Pernstich, B. Rössner, and B. Batlogg, Nat. Mater. **7**, 321 (2008).

[37] T. Ando, A. B. Fowler, and F. Stern, Rev. Mod. Phys. **54**, 437 (1982).

[38] M. S. Hybertsen and S. G. Louie, Phys. Rev. B **34**, 5390 (1986).

[39] A. Splendiani, L. Sun, Y. Zhang, T. Li, J. Kim, C.-Y. Chim, G. Galli, and F. Wang, Nano Lett. **10**, 1271 (2010).

[40] H. P. Komsa and A. V. Krasheninnikov, Phys. Rev. B **86**, 241201(R) (2012).

[41] A. Molina-Sanchez, D. Sangalli, K. Hummer, A. Marini, and L. Wirtz, Phys. Rev. B **88**, 045412 (2013).

[42] D. Y. Qiu, F. H. da Jornada, and S. G. Louie, Phys. Rev. Lett. **111**, 216805 (2013).

[43] D. Y. Qiu, F. H. da Jornada, and S. G. Louie, Phys. Rev. B **93**, 235435 (2016).

[44] J. M. Ziman, *Electrons and Phonons: The Theory of Transport Phenomena in Solids* (Clarendon, Oxford, UK, 1960).

[45] E. H. Hwang, E. Rossi, and S. Das Sarma, Phys. Rev. B **80**, 235415 (2009).

[46] N. Mohankumar and A. Natarajan, Phys. Status Solidi **188**, 635 (1995).

[47] X. Li, J. T. Mullen, Z. Jin, K. M. Borysenko, M. Buongiorno Nardelli, and K. W. Kim, Phys. Rev. B **87**, 115418 (2013).

[48] D. M. Rowe, *Materials, Preparation, and Characterization in Thermoelectrics* (Taylor & Francis, CRC Press, Boca Raton, 2012).

[49] Y. Pei, X. Shi, A. LaLonde, H. Wang, L. Chen, and G. J. Snyder, Nature **473**, 66 (2011).

[50] T. Tritt, *Recent Trends in Thermoelectric Materials Research: Part Three* (Elsevier Science, Academic Press, Cambridge, MA, 2001).

[51] P. Norouzzadeh, C. W. Myles, and D. Vashaee, Sci. Rep. **4**, 7028 (2014).

[52] D. Ovchinnikov, A. Allain, Y.-S. Huang, D. Dumcenco, and A. Kis, ACS Nano **8**, 8174 (2014).

[53] L. Li, Y. Yu, G. J. Ye, Q. Ge, X. Ou, H. Wu, D. Feng, X. H. Chen, and Y. Zhang, Nat. Nanotechnol. **9**, 372 (2014).

[54] S. J. Choi, B.-K. Kim, T.-H. Lee, Y. H. Kim, Z. Li, E. Pop, J.-J. Kim, J. H. Song, and M.-H. Bae, Nano Lett. **16**, 3969 (2016).

[55] S. Sinha and K. E. Goodson, Int. J. Multiscale Comput. Eng. **3**, 107 (2005).

[56] M. Kayyalha, J. Maassen, M. Lundstrom, L. Shi, and Y. P. Chen, J. Appl. Phys. **120**, 134305 (2016).

[57] K. L. Grosse, M.-H. Bae, F. Lian, E. Pop, and W. P. King, Nat. Nanotechnol. **6**, 287 (2011).

[58] M. Bae, Z. Ong, D. Estrada, and E. Pop, Nano Lett. **10**, 4787 (2010).